

© 2023 IEEE. Personal use of this material is permitted. Permission from IEEE must be obtained for all other uses, in any current or future media, including reprinting/republishing this material for advertising or promotional purposes, creating new collective works, for resale or redistribution to servers or lists, or reuse of any copyrighted component of this work in other works.

Citation: Song, Meiping, Lan Li, Chunyun Zhang, Pengliang Shi, Liaoying Zhao, and Bai Xue. "Subpixel Mapping of Hyperspectral Image Based on Multi-Scale and Multi-Feature." IEEE Transactions on Geoscience and Remote Sensing, 2023, 1–1. <https://doi.org/10.1109/TGRS.2023.3325825>.

DOI: <https://doi.org/10.1109/TGRS.2023.3325825>

Access to this work was provided by the University of Maryland, Baltimore County (UMBC) ScholarWorks@UMBC digital repository on the Maryland Shared Open Access (MD-SOAR) platform.

#### **Please provide feedback**

Please support the ScholarWorks@UMBC repository by emailing [scholarworks-group@umbc.edu](mailto:scholarworks-group@umbc.edu) and telling us what having access to this work means to you and why it's important to you. Thank you.

# Subpixel Mapping of Hyperspectral Image Based on Multiscale and Multifeature

Meiping Song<sup>1b</sup>, Lan Li<sup>1b</sup>, Chunyun Zhang<sup>1b</sup>, Pengliang Shi, Liaoying Zhao<sup>1b</sup>, and Bai Xue<sup>1b</sup>, *Member, IEEE*

**Abstract**—The ubiquity of mixed pixels in hyperspectral images makes it difficult for traditional classification techniques to determine the spatial distribution of land-cover classes accurately. Subpixel mapping (SPM) technology is an effective method to solve this problem. Aiming at taking the multiple scales and the spatial features into account, an SPM method based on multiscale and multifeature (MSMF) is proposed, so as to effectively improve the accuracy of SPM. First, the maximum linearization index (MLI) method of the nonredundant complete straight-line (CSL) set is designed to identify the linear distribution feature of land-cover (LC) classes. Then, different methods are applied to different spatial features and unified together finally, where the template matching iterative exchange is used for the linear distribution classes, and the multiscale spatial dependence (MSD) iterative exchange method combined with area perimeter is used for the planar distribution classes. Experiments on three remote sensing images are carried out to evaluate the performance of MSMF. The results show that the proposed method can effectively improve the accuracy of SPM.

**Index Terms**—Hyperspectral image (HSI), linear feature detection, multiscale and multifeature (MSMF), subpixel mapping (SPM).

## I. INTRODUCTION

**H**YPERSPECTRAL images (HSIs) can be captured with hundreds of spectral bands, containing rich spectral information, and recorded in pixels [1]. It has been widely used in the fields of geological analysis, environmental monitoring, agriculture, and so on. A mixed pixel is formed with different spectral properties that are present in a single pixel [1]. Mixed pixels recorded more than one (two or more) classes of mixed spectral information [2], due to the limited resolution [3], which is common in HSIs with low spatial resolution. Since mixed pixels do not belong to specific classes, it is one of the main obstacles to further improving the accuracy of land-cover (LC) classification and recognition tasks [4]. Accurately

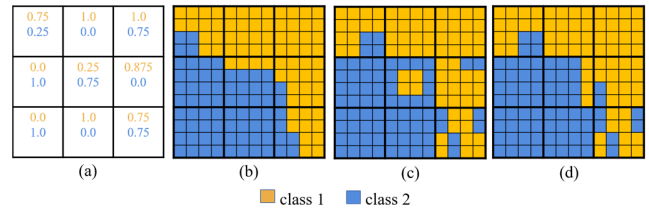


Fig. 1. Illustration of the subpixel mapping problem. (a) Fractional image. (b)–(d) Three possible class distribution maps of subpixels that satisfy the fractional constraint.

identifying and extracting LC information is significant in many applications [5], such as urban or agricultural planning [6] and disaster assessment [7].

However, mixed pixels are ubiquitous in remote sensing images, especially HSIs. Traditional classification techniques make it difficult to accurately extract LC class information. As a result, numerous techniques have been developed to tackle the issue of mixing pixels in HSIs, including soft classification [8], [9] and spectral unmixing [10]. In particular, certain methods have been developed specifically for handling mixed pixels. In [10], a kernel-based classification approach for mixed pixels is proposed. Two nonlinear mixed pixel classifiers, namely, kernel-constrained energy minimization and kernel linear-minimum variance, are designed to replace the widely used pure pixel-based support vector machine (SVM) classifiers. This type of method excels at soft classification of mixed pixels and determining the content of each class. However, when we zoom in to higher resolutions to inspect the classification results, it becomes challenging to discern the spatial distribution of subpixels within each mixed pixel, as shown in Fig. 1. This highlights that subpixel detection [12] and subpixel classification [11] differ from subpixel mapping (SPM) [1]. While the former two methods can estimate the content of each class within a mixed pixel, they cannot elucidate the specific distribution of subpixels. Fortunately, SPM can be viewed as an alternative solution. It comes into play after obtaining soft classification or performing spectral unmixing, with the goal of pinpointing the position of each subpixel class within mixed pixels to generate a finer resolution classification map.

By estimating a reasonable spatial distribution of LC classes, detailed spatial structure information in mixed pixels can be obtained [14]. The concept of SPM was first proposed in [13]. Under the relevant constraints of pixel-based soft

Manuscript received 15 May 2023; revised 19 September 2023; accepted 2 October 2023. Date of publication 19 October 2023; date of current version 1 November 2023. This work was supported in part by the National Natural Science Foundation of China under Grant 61971082 and Grant 61890964. (Corresponding authors: Liaoying Zhao; Bai Xue.)

Meiping Song is with the Guangzhou Academy of Fine Arts, Guangzhou 510260, China, and also with the Information and Technology College, Dalian Maritime University, Dalian 116026, China (e-mail: smping@163.com).

Lan Li, Chunyun Zhang, and Pengliang Shi are with the Center for Hyperspectral Imaging in Remote Sensing (CHIRS), Information and Technology College, Dalian Maritime University, Dalian 116026, China (e-mail: lanli@dlmu.edu.cn; 17806171126@163.com; spl@dlmu.edu.cn).

Liaoying Zhao is with the School of Computer Science, Hangzhou Dianzi University, Hangzhou 310018, China (e-mail: zhaoly@hdu.edu.cn).

Bai Xue is with the Department of Computer Science and Electrical Engineering, University of Maryland, Baltimore County, Baltimore, MD 21250 USA (e-mail: baixue1@umbc.edu).

Digital Object Identifier 10.1109/TGRS.2023.3325825

classification [15], [16], the mixed pixel is decomposed into subpixels, and each subpixel is assigned to a specific LC class to generate classification results with finer spatial resolution. According to the theory of spatial correlation hypothesis, a proper description of spatial dependence is the key to generating highly accurate SPM result [17].

Most of the existing SPM methods are pixel-based and are executed pixel by pixel, where the class proportions of the pixel are taken as the input, including spatial attraction models (SAMs) [18], linear optimization [19], [20], [21], and neural network-based methods [15], [22], [23]. The second type mainly includes the Hopfield neural network [24], genetic algorithm [25], and pixel-swapping algorithm (PSA) [26], which were developed mainly under the assumption of spatial dependence within and between pixels. Subsequently, Chen et al. [17] characterized the local details of LC patches by fusing the spatial dependence of pixel scale and subpixel scale, so as to obtain the best spatial distribution on subpixel scale. With the improvement of spatial resolution of remote sensing images, object-based classification has been continuously developed. Object-based classification is executed object-by-object basis in pixel-based classification. Thus, superpixel objects need to be generated first, which may result in mixed objects with multiple LC classes. Chen et al. [27] proposed an object-based SPM method based on spatial dependence theory. This method predicts the spatial arrangement within each mixed object at the subpixel scale, to solve the problem of mixed pixels in superpixel classification. This spatial dependence of object scale can well represent the structural characteristics of LC classes, but it cannot consider the local details of the LC patch, especially when the object size is large. Next, Chen et al. [28] proposed to combine the spatial dependence of object scale extracted from object-based soft classification with the spatial dependence of pixel scale and subpixel scale extracted from pixel-based soft classification, making full use of the advantages of both to predict the spatial distribution of different ground classes in mixed objects. Methods based on multiscale (MS) spatial features have achieved beneficial impacts in multiple fields [29]. However, the above method treats all LC classes as a single type, which does not consider the characteristics of feature distribution. For some typical linear features, such as roads and rivers or some short and wide linear features, segmentation may divide linear LC classes into planar areas, which will result in the loss of connectivity of linear features [30]. In considering the distribution characteristics of LC classes, Ai et al. [31] further considered the directivity and connectivity of linear features on the basis of spatial dependence and proposed an improved SPM. Thornton et al. [32] developed an SPM for more accurate super-resolution linear rural LC classes from fine spatial resolution remote sensing images. Ge et al. [30] considered the different distribution characteristics of the LC classes and adopted different SPM methods for different features, which can obtain a certain positioning effect. Xu et al. [33] considered the distribution characteristics of various LC classes, but the method needs to consider the influence of the stepping angle on the results.

In recent years, we have witnessed the great success of deep learning in various fields, such as image denoising [34], band selection [35], image fusion [36], and classification [37]. Arun et al. [38] used neural network inversion to consider texture and color information when modeling spatial correlation, which improved the generalization ability of the framework. He et al. [39] proposed a kernel-learnable convolutional neural network framework for SPM. Ma et al. [40] proposed a super-resolution convolutional neural network method to calculate subpixel soft class values through a transfer learning strategy and use a classifier to convert subpixel soft class values into hard-classified LC maps with abundance constraints. However, the performance of the deep learning approaches highly relies on the training datasets. In practice, it might be difficult to prepare synthetic datasets that adequately resemble real-world measurements covering diverse imaging conditions.

In order to solve the above problems, this article proposes an SPM algorithm based on the MS and multifeature (MSMF). First, this method takes the soft classification result on the object scale and the pixel abundance. Second, based on our previous work [41], we developed a linear feature detection method based on the nonredundant complete straight-line (CSL) set to judge the spatial distribution characteristics of the LC classes, dividing distribution features of LC classes into linear features and planar features. Finally, for LC classes with the linear feature, we improved the template matching exchange method for SPM. For LC classes with planar feature distribution, we explored the SPM method of multiscale spatial dependence (MSD) iterative exchange combined with area perimeter, which incorporates three spatial correlations of object scale, pixel scale, and subpixel scale. With the area perimeter constraint, pixels would be exchanged to improve the accuracy of SPM.

The specific contributions include the following points.

- 1) In this article, we propose a linear feature detection method based on the maximum linear index method of the nonredundant CSL (NRCSL) set to judge the linearly distributed features. This linear feature detection method can avoid the influence of the step angle  $\tau$  on the result and ensure the completeness of the number of straight line.
- 2) An MSMF-based HSI SPM method is proposed, which combines the spatial distribution characteristics of LC with MS spatial correlation and makes full use of the advantages of both to improve the accuracy of SPM.

The main structure of this article is given as follows. Section I introduces the research background and research status of SPM. Section II details the related works. Section III illustrates the proposed algorithm MSMF. The experimental result and analysis are presented in Section IV. Finally, Section IV draws conclusions.

## II. RELATED METHOD

For the convenience of description and analysis, a  $D \times D$  neighborhood grid system (NGS) with the mixed pixel  $P_{ij}$  in an image as the center is constructed, as shown in Fig. 2.  $ij$  in  $P_{ij}$  represents that the pixel  $P_{ij}$  corresponds to the center coordinates of the small square, which are  $(i+0.5, j+0.5)$ . The

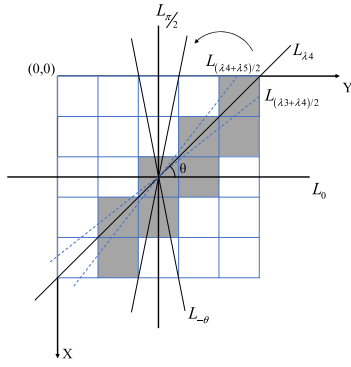


Fig. 2. Control area and linear feature detection for class  $c$  of mixed pixel  $P_{ij}$  in the new coordinate system ( $D = 5$ ).

straight lines  $L_0$  and  $L_{\pi/2}$  divide the NGS into four quadrants, and each pixel is represented by a  $1 \times 1$  grid. The pixel set of the  $D \times D$  neighborhood pixels  $P_{i'j'}$  is

$$NP_{ij} = \{P_{i'j'} | |i' - i| \leq \frac{D}{2} \wedge |j' - j| \leq \frac{D}{2}\} \quad (1)$$

where the symbol  $\wedge$  represents logical “AND.” The squares corresponding to  $P_{i'j'}$  is expressed as  $PA_{i'j'}$ , and then, the square set corresponding to all pixels in  $NP_{ij}$  is

$$\begin{aligned} AS_{ij} \\ = \{PA_{i'j'} | (i' \rightarrow (i' + 1) \wedge j' \rightarrow (j' + 1)), P_{i'j'} \in NP_{ij}\} \end{aligned} \quad (2)$$

where the symbol  $\rightarrow$  indicates the mapping relationship and  $AS_{ij}$  is the pixel control region of  $P_{i'j'}$ .

Fig. 2 shows the neighborhood pixel set  $NP_{ij}$  and linear feature detection diagram of  $P_{ij}$  in the coordinate system [33], in which the pixel grid containing the class  $c$  is marked with gray. For the convenience of description, assume that the angle from  $L_0$  to  $L_{\pi/2}$  counterclockwise along the center of  $P_{ij}$  is a positive. The angle between  $L_\theta$  and  $L_0$  is  $\theta$ . Since  $L_\theta$  and  $L_{-\theta}$  are symmetrical about the straight line  $L_0$ , the angle between  $L_0$  and  $L_{-\theta}$  is  $-\theta$ .

The maximum linearization index (MLI) is a linear feature detection mechanism proposed in [33]. In MLI, the linear mixed pixel is judged by each mixed pixel and labeled the subpixels with a linear distribution. By detecting whether the line  $L_\theta$  overlaps with the control region  $AS_{ij}$  of the pixel in  $NP_{ij}$ , the corresponding pixel set  $AL_\theta$  of the straight line  $L_\lambda$  is determined

$$AL_\theta = \{PA_{i'j'} | PA_{i'j'} \wedge L_\theta \neq \emptyset, PA_{i'j'} \in AS_{ij}\}. \quad (3)$$

For each straight line  $L_\theta$ , find the possibility of the class  $c$  with linear feature in  $P_{ij}$

$$\varphi_\theta = \frac{G_\theta(c)}{H_\theta(c)} \quad (4)$$

where  $G_\theta(c)$  is the number of pixels in set  $AL_\theta$  whose abundance of class  $c$  is greater than 0.  $H_\theta(c)$  is the number of pixels in set  $NP_{ij}$  whose abundance of class  $c$  is greater than 0 in the neighborhood pixel set.

The maximum value of all  $\varphi_\theta(c)$  corresponding to the mixed pixel  $P_{ij}$  is called the MLI, calculated as follows:

$$MLI = \varphi_{\lambda'}(c'), \exists \lambda', c' : \varphi_{\lambda'}(c') = \max\{\varphi_\lambda(c), c \in C\}. \quad (5)$$

According to the following rules:

$$MLI \geq \rho \wedge G_{\theta'}(c') \geq D \quad (6)$$

which determines whether  $P_{ij}$  has linear features. If the condition described in formula (6) is established, there is a linear feature in the pixel  $P_{ij}$ .  $\rho$  is the threshold, and the empirical value  $\rho = 0.5$ .

### III. METHODOLOGY

In order to comprehensively consider multiscale and spatial features and effectively improve the accuracy of SPM, an SPM method based on MSMF is proposed in this section. Fig. 3 shows the flowchart of the MSMF.

First, the HSI is divided into  $M$  irregular superpixel objects  $O = \{O_m | m = 1, \dots, M\}$  by simple linear iterative clustering (SLIC). The pixels in the HSI are set as  $Y = \{y_i | i = 1, \dots, N\}$ , which includes  $c$  LC classes. Each superpixel object  $O_m$  contains  $n_m$  pixels. Suppose that the zoom scale factor is  $S$ ; then, a coarse pixel will be divided into  $D \times D$  subpixel; and an object contains  $n_m \times D^2$  subpixels. According to object-based soft classification, the LC class proportion  $\{P_c(O_m) | c = 1, \dots, C\}$  based on superpixel object and the LC class proportion  $\{P_c(y_i) | c = 1, \dots, C\}$  based on pixel level are obtained. Then, the linear features are judged according to the obtained abundance map. For the linear features, we perform SPM according to the improved template matching. For the planar feature classes, we perform SPM according to the MS spatial correlation of the area perimeter. The finer spatial resolution classification result is generated by integrating the SPM of the two types of LC features.

#### A. Subpixel Mapping of Linear Feature Classes

In this section, the maximum linear index method based on the NRCSL set is proposed to detect whether there are linear feature classes in the mixed pixels. Compared with the SPM method in [41], it would avoid redundant tests but preserve the completeness of necessary solutions at the same time.

1) *Linear Feature Classes Identification by Maximum Linear Index Method Based on Nonredundant Complete Straight-Line Set*: We proposed the concept of a CSL set in our previous work [41]. However, there is redundancy in the CSL, which will increase the computational cost. Thus, how to effectively remove the redundancy of straight lines to reduce the computational time cost is the main work in this section. Here, in this article, we proposed a definition of an NRCSL set.

Fig. 4(a) shows straight lines in the third quadrant of grid control area in the central mixed pixel  $P_{ij}$  at  $D = 5$ . Connecting the vertices in the first quadrant with  $P_{ij}$ ,  $(D+1)^2/4$  straight lines can be obtained, i.e., the solid line in Fig. 4(a). The angle between these straight lines and  $L_0$  can be expressed as

$$\beta_{m,n} = \arctan\left(\frac{m+0.5}{n+0.5}\right) \quad (7)$$

where  $m = 0, (D-1)/2, n = 0, \dots, (D-1)/2$ , and  $\beta_{0,0} = \beta_{1,1} = \dots = \beta_{(D-1)/2,(D-1)/2}$ . Remove the two duplicate lines on the diagonal, making a total of  $p = (((D+1)^2)/4) - (D+1)/2 + 1$  lines. Sort the included angles of the  $p$  straight



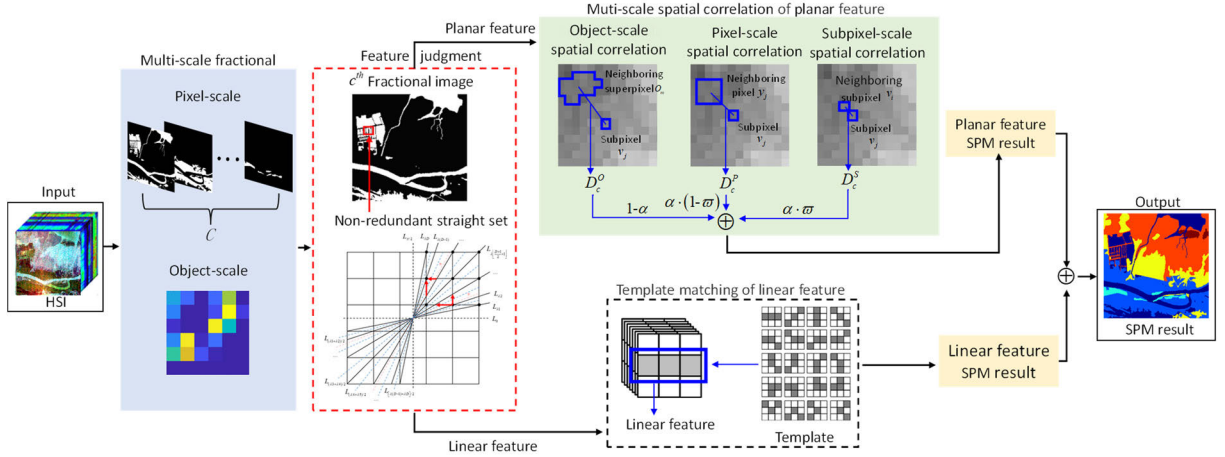
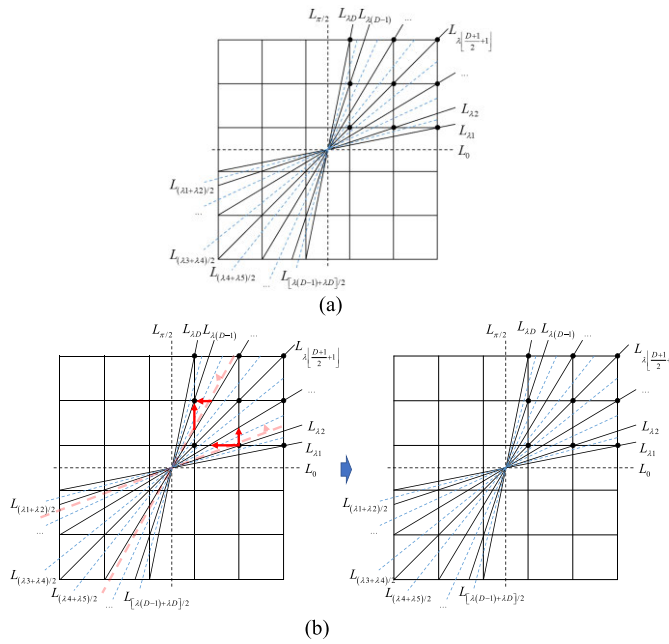


Fig. 3. Flowchart of the proposed MSMF.

Fig. 4. Set of lines for linear subpixel feature detection for class  $c$  ( $D = 5$ ). (a) Complete set of lines. (b) Nonredundant complete straight-line set.

lines from small to large, and get the included angle set  $\{\lambda_i\}$ , which satisfies  $\lambda_1 < \lambda_2 < \dots < \lambda_p$ . The squares that the  $p$  straight lines pass through are different.

Take the middle line of all black solid lines in Fig. 4(a) (blue dashed line). First, taking  $L_{\lambda_1}$  and  $L_{\lambda_2}$  as an example, a representative straight line  $L_{(\lambda_1+\lambda_2)/2}$  is taken in the interval between  $L_{\lambda_1}$  and  $L_{\lambda_2}$ , and the corresponding angle is  $(\lambda_1 + \lambda_2)/2$ . Then, do the same process to other intervals to get straight lines  $L_{(\lambda_i+\lambda_{i+1})/2}$ . In this way, a straight-line set in the first/third quadrants can be obtained. Similarly, the straight-line set in the second/fourth quadrants can be obtained according to the symmetry. Finally, the set of angles between the straight lines  $L_{\lambda}$  and  $L_0$  passing through  $P_{ij}$  is expressed as

$$\beta = \{\pm\lambda_i | i = 1, \dots, p\} \cup \left\{ \pm \frac{\lambda_j + \lambda_{j+1}}{2} | j = 1, \dots, p \right\}. \quad (8)$$

The straight lines corresponding to  $\beta$  constitute a CSL, which is used for the detection of the linear features in  $P_{ij}$ . However, there is redundancy in the CSL, which increases the computational cost to a certain extent. Taking the straight lines  $L_{\lambda_3}$  and  $L_{(\lambda_2+\lambda_3)/2}$  in Fig. 4(a) as an example, by rotating the straight line  $L_{(\lambda_2+\lambda_3)/2}$  counterclockwise, it can be seen that the pixels set, which  $L_{(\lambda_2+\lambda_3)/2}$  passed through, is the same as the straight line  $L_{\lambda_3}$ . Similarly, this phenomenon also exists for the straight lines  $L_{\lambda(D-1)}$  and  $L_{[\lambda(D-1)+\lambda(D-2)]/2}$ . This shows that although the CSL can fully cover the linear features, there is also some redundancy, which increases the time cost to a certain extent. Therefore, how to remove the redundancy in the CSL is the main work of this section.

As shown in Fig. 4(b), the straight lines, which passed the grid vertices, passed through different pixel sets. However, when the straight line enters a grid from any grid vertex and has not yet passed the new grid vertex, the pixel set that all straight lines passed is the same. Taking the straight lines  $L_{\lambda_2}$  and  $L_{\lambda_3}$  as examples, straight line  $L_{\lambda_2}$  passed a grid vertex and enters the grid to  $L_{(\lambda_2+\lambda_3)/2}$ . During this period, the straight lines did not pass through any new grid vertex and then came to  $L_{\lambda_3}$ , that is, the new vertex is reached. It can be seen that all straight lines pass through the same pixel set during this period, i.e., the straight lines  $L_{\lambda_3}$  and  $L_{(\lambda_2+\lambda_3)/2}$  passed the same grid set, so only one straight line needs to be retained.

On this basis, we generalize an angle set  $\gamma$  of straight lines for this finding.

- 1) Among the straight line before the diagonal  $L_{\lambda_{\lfloor(D+1)/2+1\rfloor}}$ , the straight line through vertex on the edge with the neighborhood straight line before it, the angle satisfies this finding.
- 2) Among the straight line after the diagonal  $L_{\lambda_{\lfloor(D+1)/2+1\rfloor}}$ , the straight line through vertex on the edge with the neighborhood straight line following it, the angle satisfies this finding.

By removing redundant straight lines, an NRCSL set  $\beta'$  is obtained

$$\beta' = \{\pm\lambda_i | i = 1, \dots, p\} \cup \left\{ \pm \frac{\lambda_j + \lambda_{j+1}}{2} | j = 1, \dots, p \right\} - \{\lambda_i | \lambda_i \in \gamma\}. \quad (9)$$

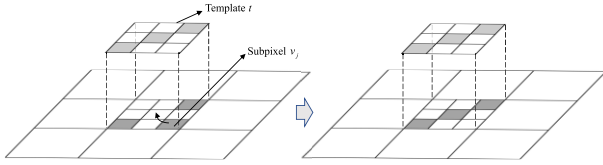


Fig. 5. Schematic of template matching exchange mapping.

Using the NRCSL and calculating the MLI according to (5), it can be judged whether  $P_{ij}$  contains linear features effectively.

2) *Subpixel Mapping of Linear Feature Class*: For the linear feature classes in the mixed pixels, a template matching [30] exchange SPM method is improved here. The defined binary template matrix  $T_k$  is expressed as follows:

$$T_k = \begin{bmatrix} t(-1, -1) & t(-1, 0) & t(-1, 1) \\ t(0, -1) & t(0, 0) & t(0, 1) \\ t(1, -1) & t(1, 0) & t(1, 1) \end{bmatrix} \quad (10)$$

where  $k = 1, 2, \dots, 20$ . Each element of the matrix  $t(m, n) \in \{0, 1\}$ ,  $m, n = (-1, 0, 1)$ , and  $k$  represents the number of templates.

The correlation coefficient is calculated to obtain the best template, and then, the best template is used to map subpixels of linear structure in  $P_{ij}$ . The exchanging principle is given as follows.

The Euclidean distance between the subpixel  $v_j$  and elements with value 1 in the optimal template is calculated within  $P_{ij}$ . Select the template element  $t$  with the smallest distance, and exchange it with subpixel  $v_j$ . Iteratively complete the SMP of linear feature classes (see Fig. 5).

### B. Subpixel Mapping of Planar Feature Classes

For the planar feature, the dependence between the LC classes is expressed by attraction on three spatial scales.

1) *Multiscale Spatial Dependence (MSD)*: The MSD of LC classes is calculated by fusing the attraction values on three spatial scales, and the perimeter of the superpixel area is used as an additional condition.

a) *Subpixel-scale spatial dependence*: Taking the  $3 \times 3$  neighborhood of subpixel  $v_j$  as the gravitational field, the calculation formula for the spatial correlation on the subpixel scale in the gravitational field is given as follows [13]:

$$D_c^S(v_j) = \frac{1}{n_1} \sum_{i=1}^{n_1} P_c(y_j) \cdot P_c(y_i) \cdot \frac{1}{d(v_j, v_i)^2}. \quad (11)$$

$P_c(y_j)$  represents the abundance of the mixed pixel  $y_j$  where the subpixel  $v_j$  of class  $c$  is located,  $y_i$  represents the mixed pixel where the adjacent subpixel  $v_i$  is located,  $d$  represents the Euclidean distance between the subpixel  $v_j$  and  $v_i$ , and  $n_1$  represents the number of subpixels in the neighborhood.

b) *Pixel-scale spatial dependence*: The SAM has been proven effective [18], and thus, it is used here to produce pixel-scale dependences of class  $c$  for subpixel  $v_j$

$$D_c^P(v_j) = \frac{1}{n_2} \sum_{i=1}^{n_2} P_c(y_i) \cdot \frac{1}{d(v_j, y_i)}. \quad (12)$$

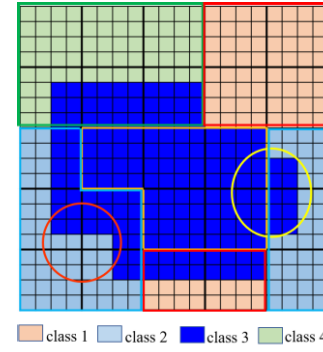


Fig. 6. Schematic of the perimeter of the connected area, different colored outlines represent different superpixels. Red and yellow circle locations indicate the attraction interaction between subpixels, pixels, and superpixels.

Among them,  $d(v_j, y_i)$  is the Euclidean distance between the subpixel  $v_j$  and the pixel  $y_i$ , and  $n_2$  is the number of adjacent pixels.

c) *Object-scale spatial dependence*: In this article, based on the SAM, we define the following formula to produce object-scale spatial dependences of class  $c$  for  $v_j$ :

$$D_c^O(v_j) = \frac{1}{n_3} \sum_{m=1}^{n_3} P_c(O_m) \cdot \frac{1}{d(v_j, O_m)} \quad (13)$$

where  $v_j$  is the subpixel in the mixed object  $O_m$ ,  $P_c(O_m)$  is the abundance of class  $c$  in the adjacent object,  $n_3$  represents the number of adjacent objects, and  $d(v_j, O_m)$  represents the Euclidean distance between the centroid of the object  $O_m$  and the subpixels  $v_j$ .

d) *Multiscale spatial dependence (MSD)*: According to the spatial dependence of object scale, pixel scale, and subpixel scale, the MSD is fused as follows:

$$D_c^M(v_j) = (1 - \alpha) \cdot D_c^O(v_j) + \alpha[(1 - \varpi) \cdot D_c^P(v_j) + \varpi \cdot D_c^S(v_j)] \quad (14)$$

where  $D_c^M(v_j)$  is the MSD of class  $c$  of the subpixel  $v_j$ .  $D_c^O(v_j)$ ,  $D_c^P(v_j)$ , and  $D_c^S(v_j)$  are the object scale, pixel scale, and subpixel scale spatial dependences of class  $c$  for subpixel  $v_j$ , respectively. The parameters  $\alpha$  and  $\varpi$  are empirically set to 0.9 and 0.89, respectively.

2) *Area Perimeter*: Due to the constraints of spatial correlation, the closer the connection between the pixels, the smaller the perimeter of the connected area [42]. Based on the spatial correlation trends of land cover, we assume that each endmember within a pixel should be spatially close to the same endmember in the surrounding pixels. In order to ensure the accuracy of the object's spatial structure and to make the SPM results more realistic, an area perimeter is introduced into the planar feature SPM. Therefore, the perimeter belonging to regions of the same class can be calculated by minimizing the cost function given below. Among them, the perimeter is the sum of each connected region composed of subpixels to class  $c$ , as shown in Fig. 6.

This cost function based on the perimeter of the connected area is

$$\text{Per}(O_k) = \sum_{c=1}^C \sum_{j=1}^K P_j^c \quad (15)$$

**Algorithm 1** MSMF

**Input:** HSI  $Y \in \mathbb{R}^N$ , zoom scale factor  $D$ .

- 1: **Initialization:** Divide  $Y$  into  $M$  super-pixel objects  $O$  by SLIC.
- 2: Calculate the soft classification  $P_c(O_m)$  and  $P_c(y_i)$ , decompose the coarse pixel and initialize random mapping.
- 3: Judge the distribution characteristics of  $LC$  classes using the non-redundant complete straight-line set  $\beta'$ .
- 4: **if** linear feature  
Perform template matching iterative exchange.
- 5: **else**
- 6: **repeat**
- 7: Calculate object scale spatial correlation  $D_c^O(v_j)$  by Eq. (11).
- 8: Calculate pixel scale spatial correlation  $D_c^P(v_j)$  by Eq. (12).
- 9: Calculate subpixel scale spatial correlation  $D_c^S(v_j)$  by Eq. (13).
- 10: Calculate the multi-scale spatial correlation  $D_c^M(v_j)$  by Eq. (14).
- 11: Calculate the area perimeter  $\text{Per}(O_k)$  by Eq. (15).
- 12: **until** convergence or exceeding maximum iterations.
- 13: **end if**
- 14: Fuse the SPM results of linear and planar distribution characteristics.
- 15: **Output:** High-resolution SPM result.

where  $c$  represents the currently compute class,  $C$  is the class number,  $K$  represents the number of connected areas of class  $c$ , and  $P_i^c$  represents the perimeter of the  $j$ th connected area of class  $c$ .

*C. MSMF Algorithm*

The algorithm of HSI SPM based on MSMF is given as follows.

## IV. EXPERIMENTS

To effectively evaluate the performance of the SPM algorithm proposed in this article, we conduct experiments on Indian pines, Pavia University, and CHRIS data (shown in Figs. 7, 10, and 13). The ground truth will be used as a reference map for qualitative and quantitative accuracy assessment. Random mapping, spatial PSA [16], spatial attraction optimization models (SAOMs) [14], linear feature detection for hyperspectral SPM (SPMLF) [41], and MSD SPM algorithm [28] are used as comparison algorithms. In order to verify the accuracy of SPM, the same method as other papers is adopted to obtain the abundance, i.e., the original image is downsampled as a pixel-level image, and the combined normalized calculation of ground-truth classes is used as the pixel abundance. To evaluate the algorithm quantitatively, the following criteria are used in the experiment, overall accuracy (OA), Kappa coefficient, classification accuracy (CA), area under the curve (AUC), receiver operating characteristic (ROC) curve [43], and average computing time  $t$ . Furthermore, it is widely acknowledged that SPM can reproduce LC information at a higher spatial resolution than observation

images. For this scale change process, the reproducibility of spatial structure in LC classes should also be considered, including the shape of the object and spatial pattern of different classes [44]. Evaluation measures based solely on CA, such as per-pixel-based or per-subpixel-based in the case of SPM, do not consider the spatial structure, and they only focus on CA. Therefore, it is necessary to include an indicator to supplement the quantitative evaluation results of SPM. Structure similarity index measure (SSIM) is generally used to measure the structural similarity between two images, and the total variation (TV) model calculates the sum of gradients between each pixel and its neighboring pixels in the image. Here, we exploit these two metrics to assess the structural characteristic and continuity of SPM results, using the ground truth as a reference image. For comparison, the best results of each quality index are labeled in boldface.

*A. Experiment on Indian Pines Data*

Indian pines dataset was obtained by the Airborne Visible/Infrared Imaging Spectrometer (AVIRIS) sensor in the north-western Indiana region of the United States in 1992. The image size is  $145 \times 145$ , containing a total of 21 025 pixels, whose spatial resolution is 20 m. The wavelength range is 0.25–2.4  $\mu\text{m}$ , and there are 220 bands. Fig. 7(a) shows the 186th band of the HSI of Purdue Indiana Indian Pine test site (Purdue's data), Fig. 7(b) shows the corresponding ground truth, and Fig. 7(c) lists the 16 real object classes and backgrounds contained in the HSI. For convenience, this experiment selects a subimage of  $135 \times 135$  size, and two scaling factors, 3 and 5, were tested.

Fig. 8 shows the SPM result ( $D = 3$ ) on Indian pines. Fig. 7(a) and (b) shows the ground truth and random mapping result, respectively. Fig. 8(c)–(h) shows the results of five SPM algorithms. In the visual effect, the random mapping results have obvious fractures and burrs in the boundary area. Compared with the results of the other four SPM methods in Fig. 8(c)–(f), the boundaries of MSMF are smoother and have a better visual effect. Specifically, there are many jagged edges and isolated points in the SPM result of PSA and SAOM. The SPM result of SPMLF has also jagged edges, but most of the edges are smoother than those of PSA and SAOM. As shown in Fig. 8(f), the SPM result of MSD is obviously better than PSA, SAOM, and SPMLF, but some small edges are not as good as those of MSMF. MSMF has smoother edges, which are closer to the reference image visually, especially on class 11. The reason is that the boundary can be seen as a linear feature when the scale is small. For example, in the edge of classes 4 and 10, MSMF has obvious superiority over MSD.

Table I lists the quantitative evaluation results of different SPM methods with scale factors of 3 and 5. MSMF achieved the best OA value in all cases. Specifically, compared with competitors, when  $D = 3$ , the OA value is 0.7% higher than the second best, and the Kappa value is 0.01 higher than the second best. When  $D = 5$ , compared with the second best, the OA value is increased by more than 1.2%, and the Kappa value is increased by more than 0.015. The TV and SSIM values also show that the proposed MSMF also performs optimally in LC information reproduction ability. According to Table I, SAOM

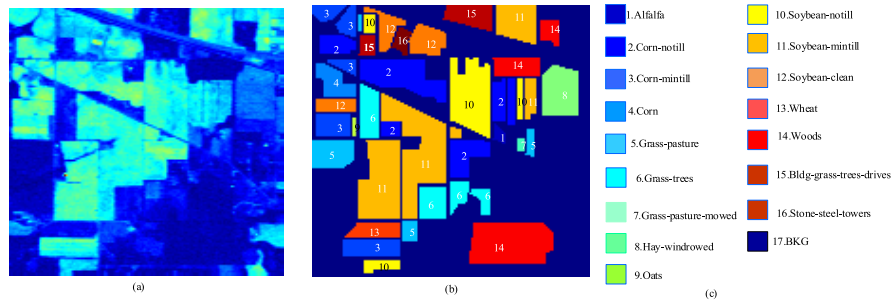


Fig. 7. Purdue's data and its ground truth with 16 classes. (a) Band 186. (b) Ground-truth map. (c) Classes by colors.

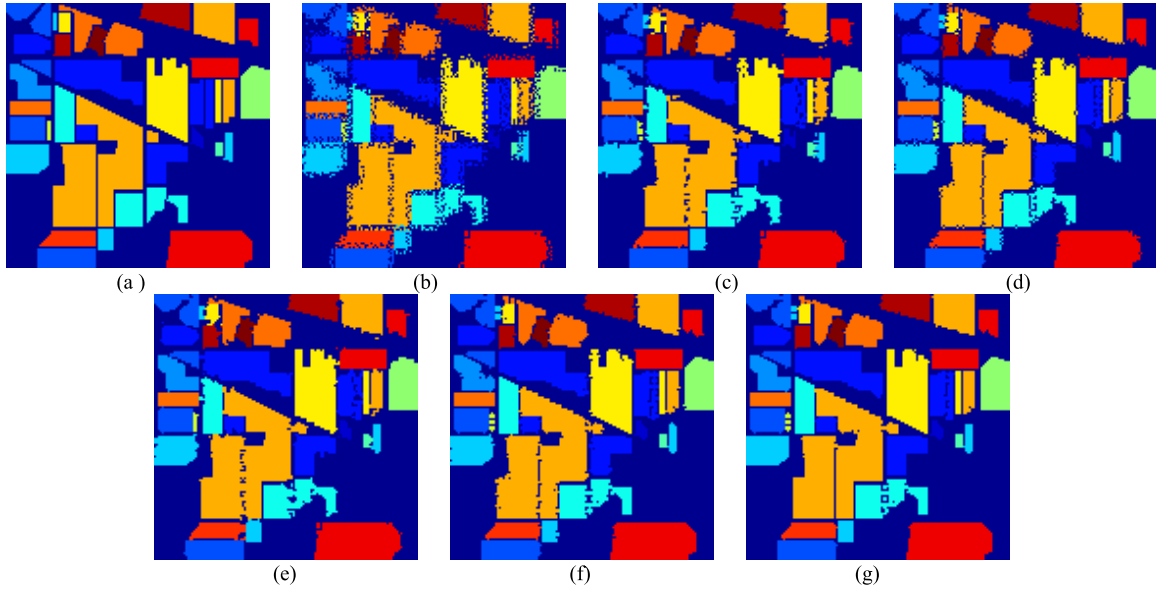


Fig. 8. SPM results for the Indian pines ( $D = 3$ ). (a) Ground truth. (b) Random. (c) PSA. (d) SAOM. (e) SPMLF. (f) MSD. (g) MSMF.

TABLE I  
OVERALL ACCURACY RESULTS OF SPM ON DIFFERENT ZOOM SCALES

	$D=3$					$D=5$				
	OA(%)	Kappa	TV	SSIM	t(s)	OA(%)	Kappa	TV	SSIM	t(s)
Random	88.78	0.8510	43128	0.4663	0.4	81.08	0.7487	59146	0.2700	0.1
PSA	96.00	0.9469	23777	0.8102	26.4	89.97	0.8669	27470	0.5132	55.4
SAOM	95.85	0.9449	28126	0.7724	1.4	90.16	0.8693	37763	0.5086	0.7
SPMLF	96.51	0.9537	22897	0.8312	19.1	89.37	0.8588	26447	0.5257	35.6
MSD	97.34	0.9648	23018	0.8512	3.5	93.74	0.9169	26555	0.6638	3.0
MSMF	<b>98.07</b>	<b>0.9744</b>	<b>21685</b>	<b>0.8967</b>	24.6	<b>94.97</b>	<b>0.9332</b>	<b>23356</b>	<b>0.7523</b>	23.9

has the shortest running time, followed by MSD. In addition, MSMF's running time is lower than that of PSA. Table II lists the SPM accuracy of each class. MSMF also achieved the best OA value in all the LC classes.

Fig. 9 shows the ROC curve [38] for each class by different SPM methods. Table III provides further evidence for the assessment of AUC values ( $D = 3$ ). From Table III, compared to competitors, MSMF is more effective and achieves the best value in almost all of the LC classes. Especially, in the classes of small objects, such as classes 4 and 7, our method achieves an obvious improvement.

#### B. Experiment on Pavia University Data

The Pavia University data are acquired by the Reflective Optics System Imaging Spectrometer (ROSIS) sensor, in the

Pavia region, Italy, in 2001. The image size is  $610 \times 340$ , containing a total of 207 400 pixels with a spatial resolution of 1.3 m. The waveband range is  $0.43\text{--}0.86 \mu\text{m}$ , and there are totally 103 bands. The image includes nine LC classes. Fig. 10(b) shows its ground truth and the labels are shown in Fig. 10(c). The spatial features at Pavia University are more obvious, especially the linear features, which can more clearly reflect the effectiveness of the algorithms. For convenience, a  $270 \times 180$  subimage is selected, and three scaling factors 3, 5, and 6 are tested. It is noticed that classes 3, 6, and 7 are not evaluated in the following experiment.

Fig. 11 shows the SPM results ( $D = 3$ ) generated by different methods, where Fig. 11(a) and (b) shows the ground truth and the random mapping result, respectively. Fig. 11(c)–(g) shows the SPM results for five algorithms of PSA, SAOM,



TABLE II  
CA RESULTING OF SPM ON INDIAN PINES ( $D = 3$ ) (%)

Class	Random	PSA	SAOM	SPMLF	MSD	MSMF
1	88.08	95.66	95.48	96.20	97.10	<b>97.90</b>
2	83.91	92.17	93.04	91.73	<b>95.65</b>	<b>95.65</b>
3	87.75	95.29	95.12	95.42	96.69	<b>97.88</b>
4	91.85	96.96	97.10	97.97	98.00	<b>98.21</b>
5	86.41	95.94	94.43	97.46	97.13	<b>98.98</b>
6	82.89	94.20	95.03	95.56	97.22	<b>98.34</b>
7	85.67	94.13	94.54	95.15	96.6301	<b>96.65</b>
8	72.14	85.71	95.71	94.28	<b>100.00</b>	<b>100.00</b>
9	93.70	98.87	98.98	99.04	99.43	<b>100</b>
10	60.00	65.00	69.00	49.00	<b>70.00</b>	<b>70.00</b>
11	88.83	96.28	96.97	97.46	98.52	<b>99.2</b>
12	90.68	96.59	95.94	97.05	96.87	<b>97.72</b>
13	88.49	96.18	96.18	96.79	97.77	<b>98.34</b>
14	86.24	97.17	94.73	95.70	98.63	<b>99.02</b>
15	95.33	99.04	98.84	99.04	99.52	<b>99.63</b>
16	86.63	96.52	96.11	96.47	97.82	<b>98.60</b>
OA	88.78	96.00	95.85	96.51	97.34	<b>98.07</b>
Kappa	0.8510	0.9469	0.9449	0.9537	0.9647	<b>0.9744</b>

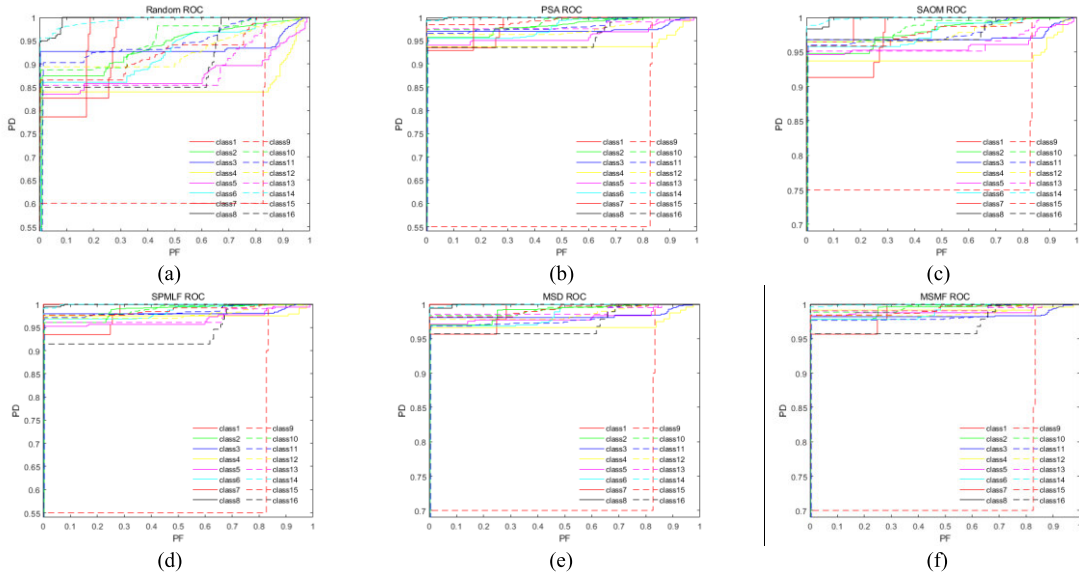


Fig. 9. ROC analysis produced by SPM for Indian pines ( $D = 3$ ). (a) Random. (b) PSA. (c) SAOM. (d) SPMLF. (e) MSD. (f) MSMF.

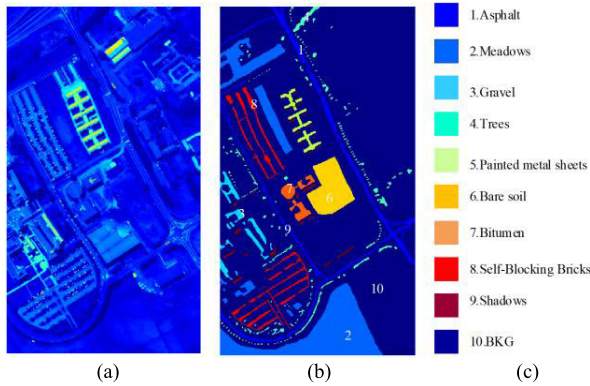


Fig. 10. Pavia University and its ground truth with nine classes. (a) Pavia University scene. (b) Ground-truth map. (c) Classes by colors.

SPMLF, MSD, and MSMF, respectively. According to Fig. 10, the edge burr phenomenon of the random mapping is serious, and the edge smoothness of PSA and SAOM is unsatisfactory.

SPMLF has some isolated points in the bottom-left corner of class 4. Visually, MSD is better than PSA, SAOM, and SPMLF, but it is still unsmoothness in some class edges, such as class 8. On the contrary, MSMF has the best edge smoothness and the fewest isolated points, achieving the best visual performance.

To provide a comprehensive quantitative evaluation, the OA and Kappa values ( $D = 3, 5, 6$ ) of the five SPM algorithms are presented in Table IV. As shown in Table IV, MSMF achieves the best values in all cases and has a pleasing improvement over the competition, which is consistent with the qualitative assessment. This shows that the MSMF is more suitable for such LC classes with a linear distribution. Therefore, MSMF achieves the best visual quality and quantitative performance for all scale factors by making full use of the MS spatial structure to retain local detail information. The optimal SSIM and TV values demonstrate the reproducibility of the presented MSMF to the shape of objects and spatial patterns of different

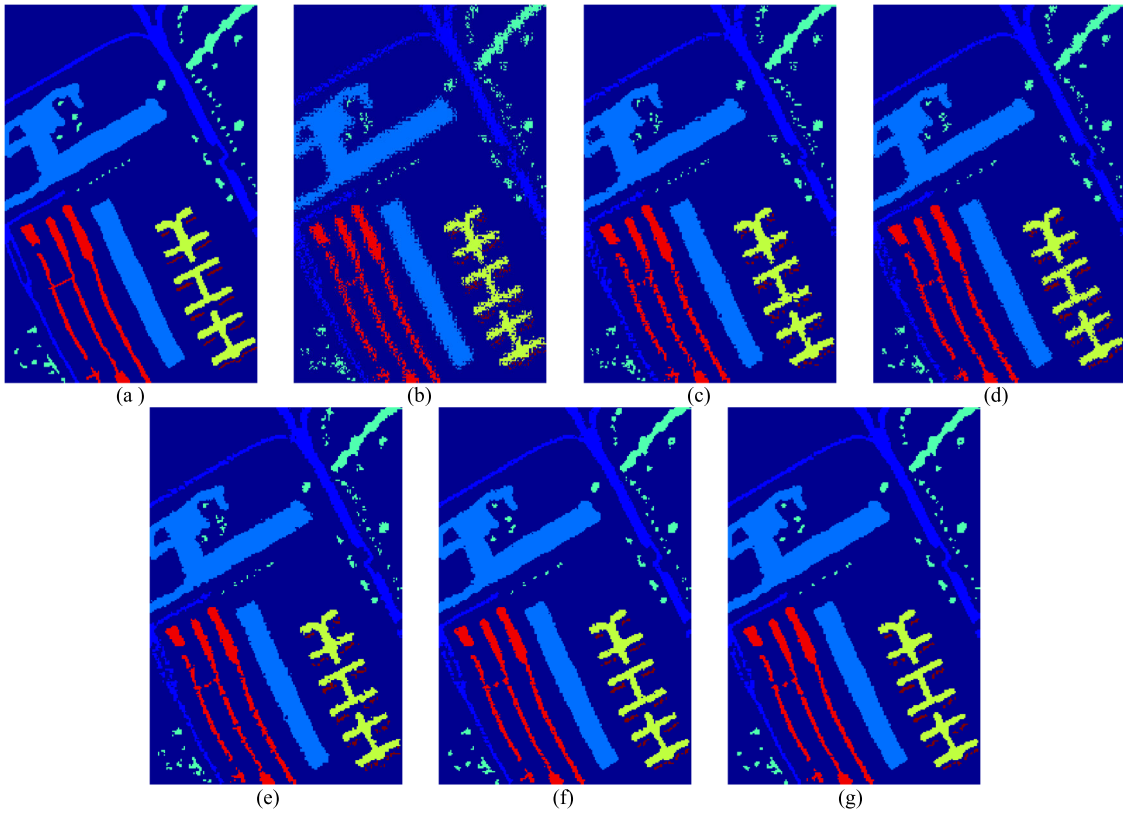


Fig. 11. SPM results for Pavia University ( $D = 3$ ). (a) Reference. (b) Random. (c) PSA. (d) SAOM. (e) SPMLF. (f) MSD. (g) MSMF.

TABLE III  
AUC VALUES FOR SINGLE CLASS ON INDIAN PINES ( $D = 3$ )

Class	Random	PSA	SAOM	SPMLF	MSD	MSMF
1	0.9461	0.9702	0.9701	0.9758	<b>0.9883</b>	<b>0.9883</b>
2	0.9352	0.9794	0.9796	0.9847	0.9867	<b>0.9913</b>
3	0.9347	0.9768	0.9782	0.9778	0.9818	<b>0.9846</b>
4	0.8530	0.9302	0.9656	0.9563	0.9734	<b>0.9883</b>
5	0.8635	0.9772	0.9607	0.9670	0.9851	<b>0.9887</b>
6	0.9086	0.9553	0.9702	0.9650	<b>0.9840</b>	0.9825
7	0.9610	0.9812	0.9937	0.9874	0.9874	<b>0.9999</b>
8	0.9950	0.9993	0.9993	0.9993	0.9997	<b>0.9999</b>
9	0.6257	0.7508	0.7095	0.5860	0.7508	<b>0.7512</b>
10	0.9516	0.9868	0.9853	0.9914	0.9907	<b>0.9969</b>
11	0.9433	0.9764	0.9757	0.9789	0.9801	<b>0.9840</b>
12	0.9222	0.9659	0.9774	0.9702	0.9843	<b>0.9891</b>
13	0.9044	0.9818	0.9697	0.9703	0.9892	<b>0.9925</b>
14	0.9906	0.9979	0.9980	0.9987	0.9991	<b>0.9993</b>
15	0.9334	0.9898	0.9865	0.9842	0.9916	<b>0.9934</b>
16	0.8811	0.9504	0.9511	0.9570	<b>0.9720</b>	<b>0.9720</b>
AVG	0.9093	0.9606	0.9607	0.9531	0.9715	<b>0.9751</b>

classes. In addition, by horizontally comparing the OA values under the three scale factors in Table IV, MSMF is 6.6% higher than random mapping with  $D = 6$ , 7% with  $D = 5$ , and 6.1% with  $D = 3$ . The improvement is the biggest with  $D = 5$ , but the accuracy is the highest when  $D = 3$ . It means that with scale factor increasing, the performance of the algorithms degrades. Similarly, in terms of the average time  $t$ , SAOM has the least running time, followed by MSD. Also, MSMF is less than SPMLF and PSA.

Table V lists the OA results ( $D = 3$ ) of the six LC classes in Pavia University data. It is obvious that MSMF achieves

the best performance on all classes, and the OA and Kappa values are optimal as well. Fig. 12 shows a comparison of the ROC curves in each class by different SPM methods. Table VI provides evidence for the assessment of AUC values ( $D = 3$ ). As shown in Table VI, compared to competitors, MSMF is obviously superior and achieves the best value in all of the LC classes. Especially in classes 1, 2, and 8, the improvement is more significant.

### C. CHRIS Image Experiment

CHRIS HSI is used to demonstrate the effectiveness of the proposed method, with size  $512 \times 512 \times 18$ . The spectral range is 406–1036 nm, and the spectral resolution of each band and spatial resolution are 5.8–44.1 and 17 m, respectively. The ground-truth and class labels are shown in Fig. 13(b) and (c), respectively. For convenience, a  $510 \times 510 \times 18$  subimage is used, and three scaling factors 3, 5, and 6, were tested.

Fig. 14 shows the SPM results ( $D = 3$ ) generated by different algorithms on CHRIS data, where Fig. 14(a) shows the reference map and Fig. 14(b)–(g) shows the SPM results for random mapping, PSA, SAOM, SPMLF, MSD, and MSMF, respectively. Visually, PSA, SAOM, and SPMLF have more obvious jagged and isolated points than MSD and MSMF. Fig. 14 (b1)–(g1) shows the details of the linear feature *Spartina alterniflora* class on the left of the SPM result. According to Fig. 14(b1)–(g1), MSMF has obvious superiority over MSD, PSA, SAOM, and SPMLF, which can restore the linear features of the beach class more accurately, and the generated spatial structure is more similar to the reference

TABLE IV  
OVERALL ACCURACY RESULTS OF SPM ON DIFFERENT ZOOM SCALES

	$D=3$					$D=5$					$D=6$				
	OA(%)	Kappa	TV	SSIM	t(s)	OA(%)	Kappa	TV	SSIM	t/s	OA(%)	Kappa	TV	SSIM	t(s)
Random	92.06	0.7980	38423	0.5268	1.4	87.51	0.6820	49504	0.3480	0.4	85.53	0.6316	53381	0.3051	0.3
PSA	95.69	0.8903	25125	0.7320	179.5	92.97	0.8211	25347	0.5797	280.8	91.14	0.7747	26188	0.5040	344.6
SAOM	96.22	0.9038	26394	0.7550	<b>3.0</b>	92.11	0.7991	32432	0.5451	<b>1.5</b>	89.86	0.7419	38096	0.4521	<b>1.7</b>
SPMLF	96.56	0.9125	23729	0.7779	141.5	92.40	0.8067	23864	0.5739	232.0	90.07	0.7473	25008	0.4739	271.1
MSD	97.88	0.9461	22419	0.8567	8.2	93.70	0.8398	27201	0.5985	7.6	91.08	0.7731	31146	0.4840	8.8
MSMF	<b>98.15</b>	<b>0.9530</b>	<b>21315</b>	<b>0.8696</b>	54.3	<b>94.40</b>	<b>0.8576</b>	<b>22341</b>	<b>0.6693</b>	96.5	<b>92.10</b>	<b>0.7990</b>	<b>23982</b>	<b>0.5604</b>	110.7

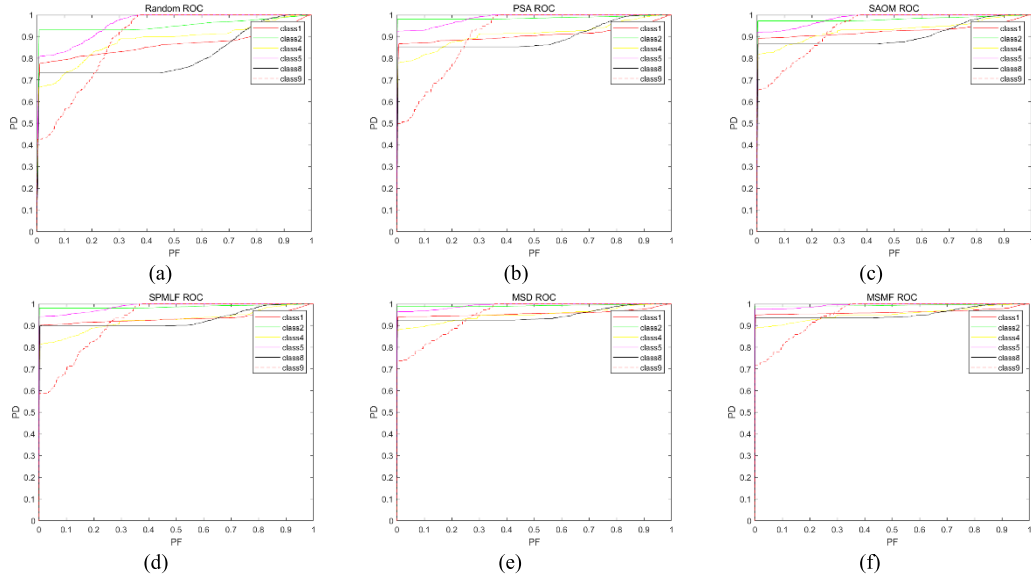


Fig. 12. ROC analysis produced by SPM for Pavia University ( $D = 3$ ). (a) Random. (b) PSA. (c) SAOM. (d) SPMLF. (e) MSD. (f) MSMF.

TABLE V  
CA RESULTING OF SPM ON PAVIA UNIVERSITY ( $D = 3$ ) (%)

Class	Random	PSA	SAOM	SPMLF	MSD	MSMF
1	94.84	97.19	97.54	97.76	98.62	<b>98.80</b>
2	77.55	86.87	88.81	90.26	94.15	<b>95.15</b>
4	92.91	97.83	97.35	97.94	98.79	<b>99.07</b>
5	64.89	75.97	80.83	80.04	87.68	<b>88.31</b>
8	80.68	91.91	91.79	93.82	96.17	<b>97.42</b>
9	73.54	85.04	87.10	88.88	92.59	<b>93.40</b>
OA	92.06	95.69	96.22	96.56	97.88	<b>98.15</b>
Kappa	0.7980	0.8903	0.9038	0.9125	0.9461	<b>0.9531</b>

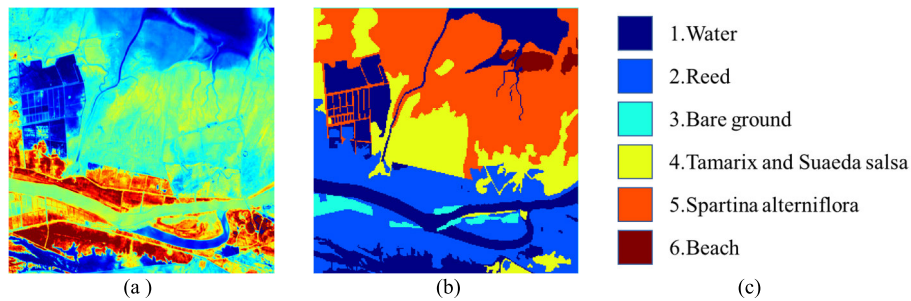


Fig. 13. CHRIS and its ground truth with six classes. (a) CHRIS scene. (b) Ground-truth map. (c) Classes by colors.

image. In addition, it can be seen from Fig. 14 that MSMF has smoother and continuous class boundaries, which are overall closer to the reference map. This is because the boundaries can be viewed as a form of linear features to some extent. This demonstrates the superiority of our proposed MSMF method.



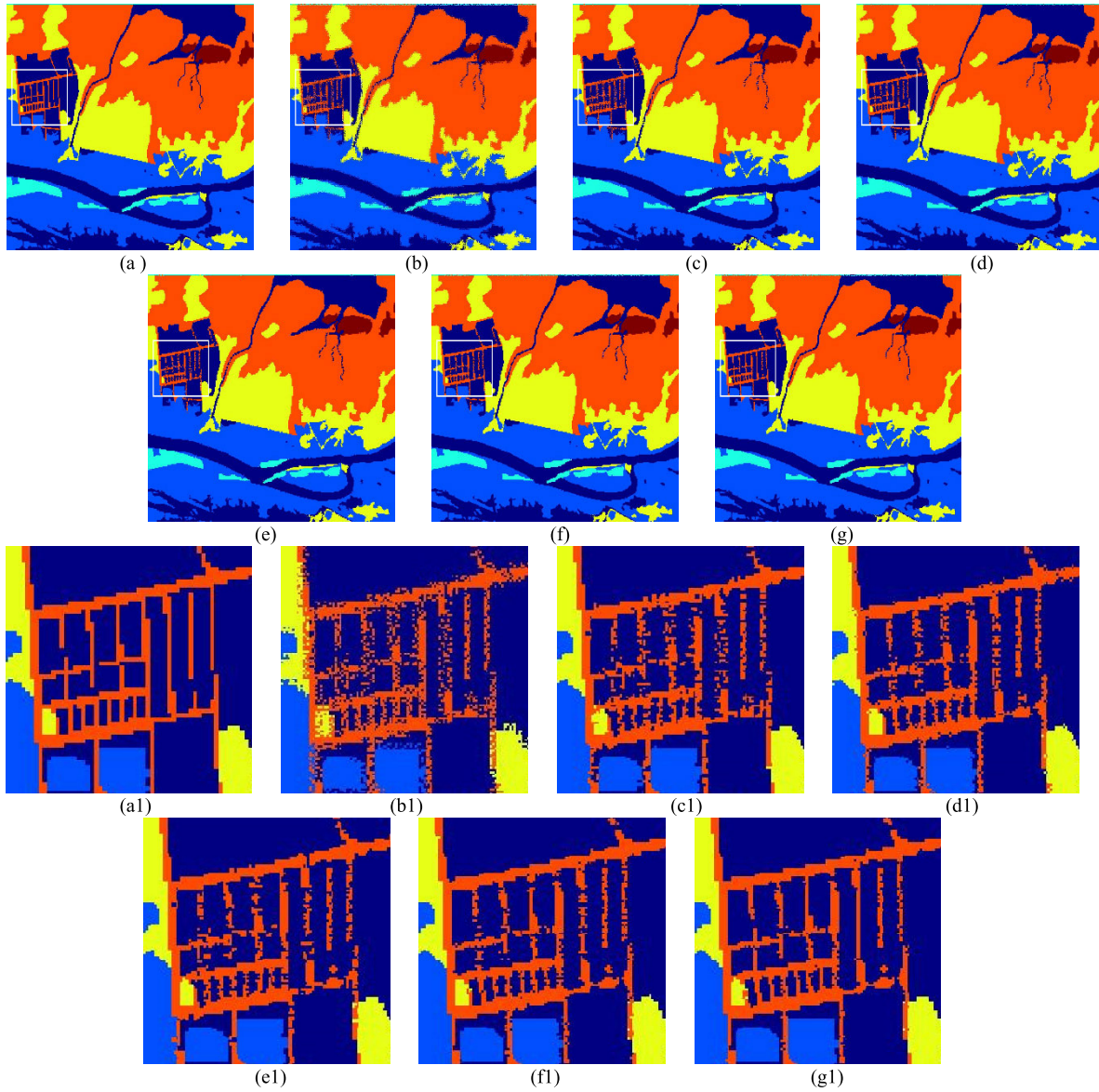


Fig. 14. SPM results of CHRIS ( $D = 3$ ). (a) Reference. (b) Random. (c) PSA. (d) SAOM. (e) SPMLF. (f) MSD. (g) MSMF. (a1)–(g1) Enlarged images in the white boxed areas of (a)–(g), respectively.

TABLE VI

AUC VALUES FOR SINGLE CLASS ON PAVIA UNIVERSITY ( $D = 3$ )

Class	Random	PSA	SAOM	SPMLF	MSD	MSMF
1	0.8618	0.9076	0.9267	0.9322	0.9564	<b>0.9629</b>
2	0.9500	0.9854	0.9800	0.9862	0.9916	<b>0.9933</b>
4	0.8799	0.9099	0.9290	0.9238	0.9493	<b>0.9522</b>
5	0.9587	0.9837	0.9823	0.9869	0.9921	<b>0.9942</b>
8	0.8121	0.8964	0.9059	0.9279	0.9473	<b>0.9538</b>
9	0.8889	0.9071	0.9360	0.9253	0.9506	<b>0.9530</b>
AVG	0.9279	0.9544	0.9622	0.9647	0.9764	<b>0.9788</b>

Table VII shows the OA and Kappa values for different SPM methods at three scale factors, 3, 5, and 6. Table VIII lists the PCA results ( $D = 3$ ) of the six LC classes in the CHRIS image. As shown in Table VII, the OA and Kappa values of the proposed MSMF have achieved the best values on the three-scale factors. It means that MSMF is the best on both OA

and Kappa values, which is followed by MSD. It illustrates the effectiveness of MS SPM. However, due to the addition of the multifeature strategy in MSMF, for different feature types, divide and conquer, the MSMF has higher accuracy than MSD. Furthermore, the developed MSMF exhibits the highest TV and SSIM at  $D = 3$  and achieves the highest SSIM at  $D = 5$  and  $D = 6$ . According to the time index, SAOM exhibits the shortest running time compared to other algorithms, followed by MSD. MSMF requires more computation time due to its complex framework. Nevertheless, the additional time invested in MSMF computation results in higher accuracy and interpretability, as confirmed by the quantitative evaluation metrics.

As shown in Table IX, MSMF almost all achieves the best performance on PCA results. Fig. 15 shows a comparison of the ROC curves in each class by different SPM methods. Table IX shows the AUC values on each class of different SPM methods. Likewise, MSMF has certain advantages compared



TABLE VII  
OVERALL ACCURACY RESULTS OF SPM ON DIFFERENT ZOOM SCALES

	$D=3$					$D=5$					$D=6$				
	OA(%)	Kappa	TV	SSIM	t(s)	OA(%)	Kappa	TV	SSIM	t/s	OA(%)	Kappa	TV	SSIM	t(s)
Random	95.08	0.9349	82396	0.8864	4.6	91.82	0.8918	99877	0.6839	1.9	90.35	0.8724	123550	0.6700	1.6
PSA	98.06	0.9744	47833	0.9530	1707.9	95.82	0.9447	45321	0.8237	2849.8	94.53	0.9278	54685	0.8253	3550.2
SAOM	97.99	0.9734	50592	0.9610	<b>94.7</b>	95.59	0.9417	66657	0.8307	<b>47.1</b>	93.95	0.9200	81461	0.8268	<b>38.1</b>
SPMLF	98.36	0.9784	45443	0.9626	1683.5	95.61	0.9420	<b>43670</b>	0.7959	2821.3	94.03	0.9211	<b>53066</b>	0.7984	3309.5
MSD	98.58	0.9813	44004	0.9722	193.0	96.45	0.9531	58782	0.8592	311.9	95.11	0.9353	65193	0.8624	465.3
MSMF	<b>98.77</b>	<b>0.9837</b>	<b>42655</b>	<b>0.9753</b>	1993.4	<b>96.82</b>	<b>0.9580</b>	50310	<b>0.8648</b>	3506.0	<b>95.49</b>	<b>0.9404</b>	55650	<b>0.8746</b>	4110.7

TABLE VIII  
CA RESULTING OF SPM ON CHRIS ( $D = 3$ ) (%)

Class	Random	PSA	SAOM	SPMLF	MSD	MSMF
1	93.16	0.96.90	96.91	97.39	97.83	<b>98.14</b>
2	96.03	0.98.50	98.38	98.73	98.95	<b>99.08</b>
3	88.58	0.97.88	97.08	98.02	<b>97.01</b>	96.80
4	94.87	0.98.30	98.11	98.58	98.73	<b>98.89</b>
5	96.29	0.98.39	98.42	98.63	98.84	<b>99.03</b>
6	93.23	0.97.87	97.40	98.21	98.52	<b>98.65</b>
OA	98.77	98.06	97.99	98.36	98.58	<b>98.77</b>
Kappa	0.9349	0.9744	0.9734	0.9784	0.9813	<b>0.9837</b>

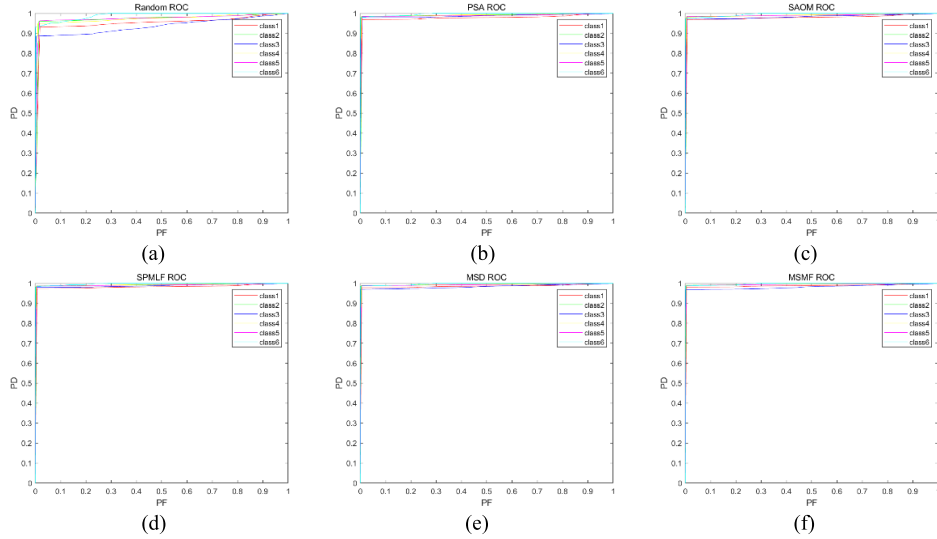


Fig. 15. ROC analysis produced by SPM of CHRIS ( $D = 3$ ). (a) Random. (b) PSA. (c) SAOM. (d) SPMLF. (e) MSD. (f) MSMF.

TABLE IX  
AUC VALUES FOR SINGLE CLASS OF DIFFERENT SPM METHODS ( $D = 3$ )

Class	Random	PSA	SAOM	SPMLF	MSD	MSMF
1	0.9508	0.9767	0.9773	0.9808	0.9841	<b>0.9867</b>
2	0.9713	0.9891	0.9882	0.9907	0.9923	<b>0.9932</b>
3	0.9360	0.9876	0.9834	<b>0.9887</b>	0.9833	0.9816
4	0.9705	0.9906	0.9896	0.9922	0.9933	<b>0.9940</b>
5	0.9735	0.9880	0.9886	0.9900	0.9916	<b>0.9931</b>
6	0.9896	0.9966	0.9956	<b>0.9975</b>	0.9974	<b>0.9975</b>
AVG	0.9653	0.9881	0.9871	0.9900	0.9903	<b>0.9910</b>

with its competitors. Combining the results of the above visual quality and quantitative analysis, the proposed MSMF achieves the best performance by fusing the different distribution features of LC classes and the spatial correlation on three scales together.

TABLE X  
ABLATION EXPERIMENT ON INDIAN PINES

	$D=3$		$D=5$	
	OA(%)	Kappa	OA(%)	Kappa
MS	97.12	0.9615	91.16	0.8825
MF	96.51	0.9537	89.37	0.8588
MSMF	<b>98.08</b>	<b>0.9744</b>	<b>94.97</b>	<b>0.9332</b>

#### D. Ablation Experiment

To verify the effectiveness of each module in the proposed MSMF SPM method, we add the corresponding ablation experiments for verification.

Tables X–XII show the ablation experiments on three data with different scaling factors, where MS is the SPM with only MS modules, MF is the SPM with only multifeature modules, and MSMF is the proposed MSMF SPM method. It can be seen from Tables X to XII that the proposed method

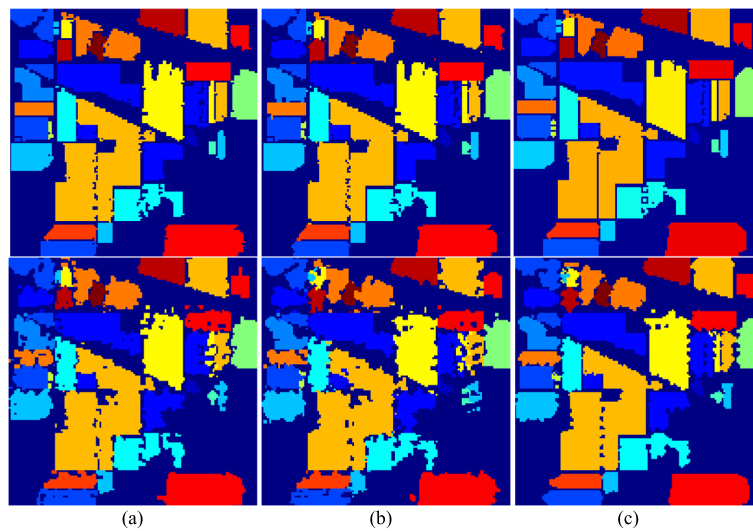


Fig. 16. SPM result of the ablation experiment on the Indian Pines dataset. (a) SPM results of MS. (b) SPM results of MF. (c) SPM results of MSMF. The first row corresponds to  $D = 3$ , and the second row corresponds to  $D = 5$ .

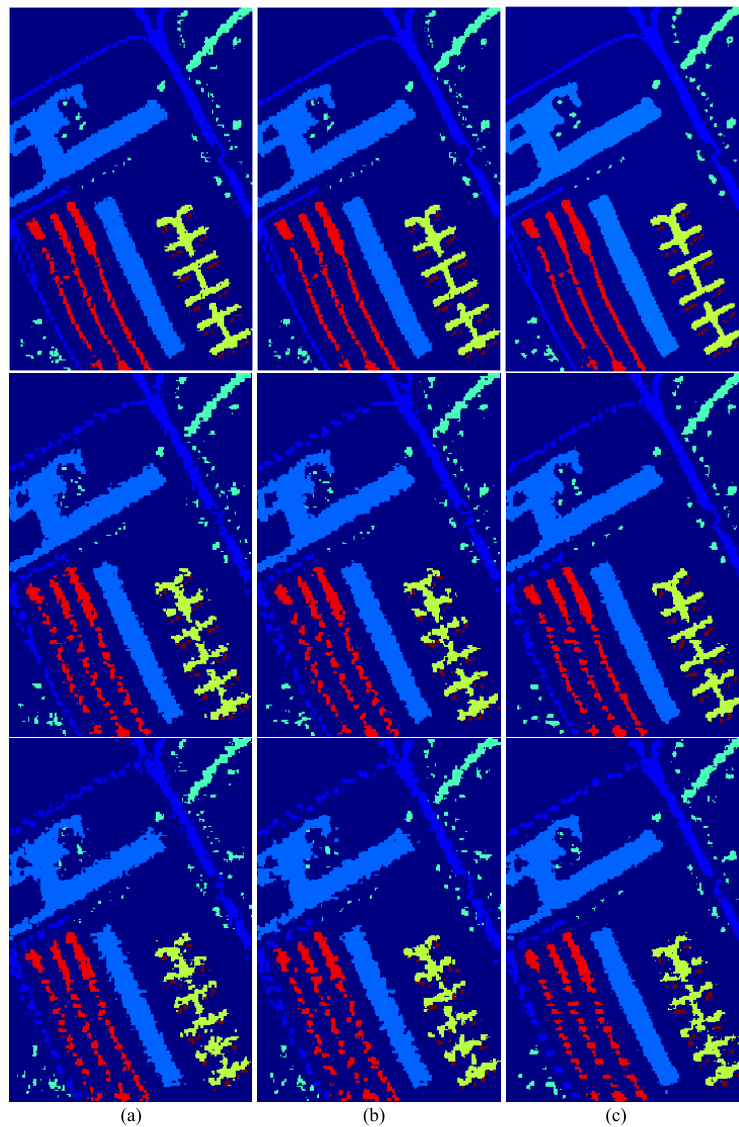


Fig. 17. SPM result of the ablation experiment on the Pavia University dataset. (a) SPM results of MS. (b) SPM results of MF. (c) SPM results of MSMF. The 1–3 row corresponds to  $D = 3$ ,  $D = 5$ , and  $D = 6$ .

is comparable in all experiments with different scaling factors and different data. Figs. 16–18 show the corresponding SPM results of ablation experiments for three datasets at different scales. From the SPM results, it is observed that MSMF

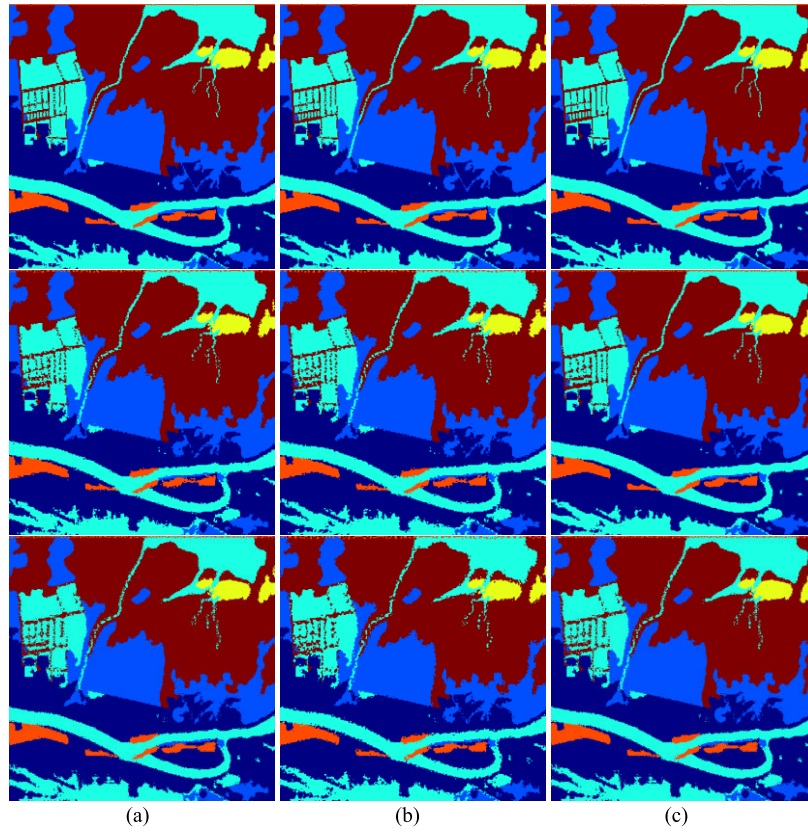


Fig. 18. SPM result of the ablation experiment on the CHRIS dataset. (a) SPM results of MS. (b) SPM results of MF. (c) SPM results of MSMF. The 1–3 row corresponds to  $D = 3$ ,  $D = 5$ , and  $D = 6$ .

TABLE XI  
ABLATION EXPERIMENT ON PAVIA UNIVERSITY

	$D=3$		$D=5$		$D=6$	
	OA(%)	Kappa	OA(%)	Kappa	OA(%)	Kappa
MS	96.77	0.9177	92.51	0.8092	90.05	0.7467
MF	96.56	0.9125	92.41	0.8067	90.08	0.7473
MSMF	<b>98.16</b>	<b>0.9530</b>	<b>94.41</b>	<b>0.8576</b>	<b>92.10</b>	<b>0.7990</b>

TABLE XII  
ABLATION EXPERIMENT ON CHRIS

	$D=3$		$D=5$		$D=6$	
	OA(%)	Kappa	OA(%)	Kappa	OA(%)	Kappa
MS	98.64	0.9821	95.94	0.9463	94.64	0.9201
MF	98.36	0.9784	95.62	0.9420	94.04	0.9211
MSMF	<b>98.77</b>	<b>0.9837</b>	<b>96.82</b>	<b>0.9580</b>	<b>95.50</b>	<b>0.9404</b>

exhibits smoother boundaries compared to the single MS or MF. It is more obvious at the edge area of Indian planes and Pavia University dataset and the linear feature area in the CHRIS dataset because edges can be considered as linear features. For the linear features, multiscale and multifeature processing of MSMF can better preserve the spatial structure of the data.

## V. CONCLUSION

This article presents an SPM method based on MSMF, aiming to combine the advantages of multiscale spatial correlation with different distribution features of land-cover classes. First, pixel- and object-based soft classifications are performed. Second, a linear feature detection method based on

a nonredundant complete linear set is defined to judge the LC classes. Then, a template matching iterative algorithm is used to find the best template for the linear feature classes. Also, MS spatial correlation is calculated by MS fusion for planar feature classes. The proposed method not only avoids the shortcomings of traditional SPM that do not consider the overall spatial structure but also consider the structural features at the object scale and the local details of pixels and subpixels. The experimental results on multiple data validate the superiority of the proposed MSMF. The quantitative evaluation of OA, Kappa coefficient, and ROC curve further shows the effectiveness of MSMF. These all prove the potential of MSMF for the SPM in remote sensing images.

## REFERENCES

- [1] M. Song, Y. Zhong, A. Ma, X. Xu, and L. Zhang, "A joint spectral unmixing and subpixel mapping framework based on multiobjective optimization," *IEEE Trans. Geosci. Remote Sens.*, vol. 60, 2022, Art. no. 5519217.
- [2] P. Fisher, "The pixel: A snare and a delusion," *Int. J. Remote Sens.*, vol. 18, no. 3, pp. 679–685, Feb. 1997.
- [3] J. Zhou, W. Sun, X. Meng, G. Yang, K. Ren, and J. Peng, "Generalized linear spectral mixing model for spatial-temporal-spectral fusion," *IEEE Trans. Geosci. Remote Sens.*, vol. 60, 2022, Art. no. 5533216.
- [4] S. Wu et al., "Influence of reconstruction scale, spatial resolution and pixel spatial relationships on the sub-pixel mapping accuracy of a double-calculated spatial attraction model," *Remote Sens. Environ., Interdiscipl. J.*, vol. 210, pp. 345–361, Jun. 2018.
- [5] M. Song, Y. Zhong, A. Ma, X. Xu, and L. Zhang, "Multiobjective subpixel mapping with multiple shifted hyperspectral images," *IEEE Trans. Geosci. Remote Sens.*, vol. 58, no. 11, pp. 8176–8191, Nov. 2020.
- [6] A. K. Shackelford and C. H. Davis, "A hierarchical fuzzy classification approach for high-resolution multispectral data over urban areas," *IEEE Trans. Geosci. Remote Sens.*, vol. 41, no. 9, pp. 1920–1932, Sep. 2003.
- [7] S. Voigt, T. Kemper, T. Riedlinger, R. Kiefl, K. Scholte, and H. Mehl, "Satellite image analysis for disaster and crisis-management support," *IEEE Trans. Geosci. Remote Sens.*, vol. 45, no. 6, pp. 1520–1528, Jun. 2007.
- [8] C.-I. Chang and K. Y. Ma, "Band sampling of kernel constrained energy minimization using training samples for hyperspectral mixed pixel classification," *IEEE Trans. Geosci. Remote Sens.*, vol. 60, 2022, Art. no. 5522721.
- [9] K. Y. Ma and C.-I. Chang, "Iterative training sampling coupled with active learning for semisupervised spectral-spatial hyperspectral image classification," *IEEE Trans. Geosci. Remote Sens.*, vol. 59, no. 10, pp. 8672–8692, Oct. 2021.
- [10] L. Ren, D. Hong, L. Gao, X. Sun, M. Huang, and J. Chanussot, "Orthogonal subspace unmixing to address spectral variability for hyperspectral image," *IEEE Trans. Geosci. Remote Sens.*, vol. 61, 2023, Art. no. 5501713.
- [11] K. Y. Ma and C.-I. Chang, "Kernel-based constrained energy minimization for hyperspectral mixed pixel classification," *IEEE Trans. Geosci. Remote Sens.*, vol. 60, 2022, Art. no. 5510723.
- [12] X. Wang et al., "A double dictionary-based nonlinear representation model for hyperspectral subpixel target detection," *IEEE Trans. Geosci. Remote Sens.*, vol. 60, 2022, Art. no. 5524516.
- [13] P. M. Atkinson, M. E. J. Cutler, and H. Lewis, "Mapping sub-pixel proportional land cover with AVHRR imagery," *Int. J. Remote Sens.*, vol. 18, no. 4, pp. 917–935, Mar. 1997.
- [14] W. Han, Q. Tian, and Y. Lu, "Spatial attraction algorithm for sub-pixel mapping of multispectral remote sensing images," *Acta Geodaetica et Cartographica Sinica*, vol. 40, no. 2, pp. 169–174, Apr. 2011.
- [15] X. Xu, Y. Zhong, L. Zhang, and P. Li, "A sub-pixel mapping algorithm based on BP neural network with spatial autocorrelation function for remote sensing imagery," *Acta Geodaetica et Cartographica Sinica*, vol. 40, no. 3, pp. 307–311, Jun. 2011.
- [16] P. M. Atkinson, "Sub-pixel target mapping from soft-classified, remotely sensed imagery," *Photogramm. Eng. Remote Sens.*, vol. 71, no. 7, pp. 839–846, Jul. 2005.
- [17] Y. Chen, Y. Ge, Q. Wang, and Y. Jiang, "A subpixel mapping algorithm combining pixel-level and subpixel-level spatial dependences with binary integer programming," *Remote Sens. Lett.*, vol. 5, no. 10, pp. 902–911, Oct. 2014.
- [18] K. C. Mertens, B. de Baets, L. P. C. Verbeke, and R. R. de Wulf, "A sub-pixel mapping algorithm based on sub-pixel/pixel spatial attraction models," *Int. J. Remote Sens.*, vol. 27, no. 15, pp. 3293–3310, Feb. 2007.
- [19] S. Chen, X. Li, and L. Zhao, "Subpixel mapping method of hyperspectral images based on modified binary quantum particle swarm optimization," *J. Electr. Comput. Eng.*, vol. 2017, pp. 1–17, Aug. 2017.
- [20] A. Ertürk, M. K. Güllü, D. Çesmeçi, D. Gerçek, and S. Ertürk, "Spatial resolution enhancement of hyperspectral images using unmixing and binary particle swarm optimization," *IEEE Geosci. Remote Sens. Lett.*, vol. 11, no. 12, pp. 2100–2104, Dec. 2014.
- [21] J. Verhoeve and R. De Wulf, "Land cover mapping at sub-pixel scales using linear optimization techniques," *Remote Sens. Environ.*, vol. 79, no. 1, pp. 96–104, Jan. 2002.
- [22] K. Wu, R. Niu, P. Li, and L. Zhang, "Sub-pixel mapping of remote sensing images based on fuzzy ARTMAP neural network model," *Geomatics Inf. Sci. Wuhan Univ.*, vol. 34, no. 3, pp. 287–300, Mar. 2009.
- [23] W. Z. Shi, Y. L. Zhao, and Q. M. Wang, "Sub-pixel mapping based on BP neural network with multiple shifted remote sensing images," *J. Infr. Millim. Waves*, vol. 33, no. 5, pp. 527–532, Nov. 2014.
- [24] A. J. Tatem, H. G. Lewis, P. M. Atkinson, and M. S. Nixon, "Super-resolution target identification from remotely sensed images using a Hopfield neural network," *IEEE Trans. Geosci. Remote Sens.*, vol. 39, no. 4, pp. 781–796, Apr. 2001.
- [25] X. Tong et al., "A new genetic method for subpixel mapping using hyperspectral images," *IEEE J. Sel. Topics Appl. Earth Observ. Remote Sens.*, vol. 9, no. 9, pp. 4480–4491, Sep. 2016.
- [26] T. Kasetkasem, M. Arora, and P. Varshney, "Super-resolution land cover mapping using a Markov random field based approach," *Remote Sens. Environ.*, vol. 96, nos. 3–4, pp. 302–314, Jun. 2005.
- [27] Y. Chen, Y. Ge, G. B. M. Heuvelink, R. An, and Y. Chen, "Object-based superresolution land-cover mapping from remotely sensed imagery," *IEEE Trans. Geosci. Remote Sens.*, vol. 56, no. 1, pp. 328–340, Jan. 2018.
- [28] Y. Chen, Y. Ge, Y. Chen, Y. Jin, and R. An, "Subpixel land cover mapping using multiscale spatial dependence," *IEEE Trans. Geosci. Remote Sens.*, vol. 56, no. 9, pp. 5097–5106, Sep. 2018.
- [29] W. Sun et al., "A multiscale spectral features graph fusion method for hyperspectral band selection," *IEEE Trans. Geosci. Remote Sens.*, vol. 60, 2022, Art. no. 5513712.
- [30] Y. Ge, Y. Chen, A. Stein, S. Li, and J. Hu, "Enhanced subpixel mapping with spatial distribution patterns of geographical objects," *IEEE Trans. Geosci. Remote Sens.*, vol. 54, no. 4, pp. 2356–2370, Apr. 2016.
- [31] B. Ai, X. Liu, G. Hu, and X. Li, "Improved sub-pixel mapping method coupling spatial dependence with directivity and connectivity," *IEEE J. Sel. Topics Appl. Earth Observ. Remote Sens.*, vol. 7, no. 12, pp. 4887–4896, Dec. 2014.
- [32] M. W. Thornton, P. M. Atkinson, and D. A. Holland, "A linearised pixel-swapping method for mapping rural linear land cover features from fine spatial resolution remotely sensed imagery," *Comput. Geosci.*, vol. 33, no. 10, pp. 1261–1272, Oct. 2007.
- [33] X. Xu, Y. Zhong, and L. Zhang, "Adaptive subpixel mapping based on a multiagent system for remote-sensing imagery," *IEEE Trans. Geosci. Remote Sens.*, vol. 52, no. 2, pp. 787–804, Feb. 2014.
- [34] Q. Zhang, Y. Zheng, Q. Yuan, M. Song, H. Yu, and Y. Xiao, "Hyperspectral image denoising: From model-driven, data-driven, to model-data-driven," *IEEE Trans. Neural Netw. Learn. Syst.*, early access, Jun. 6, 2023, doi: [10.1109/TNNLS.2023.3278866](https://doi.org/10.1109/TNNLS.2023.3278866).
- [35] K. He et al., "A dual global-local attention network for hyperspectral band selection," *IEEE Trans. Geosci. Remote Sens.*, vol. 60, 2022, Art. no. 5527613.
- [36] W. Sun et al., "MLR-DBPFN: A multi-scale low rank deep back projection fusion network for anti-noise hyperspectral and multispectral image fusion," *IEEE Trans. Geosci. Remote Sens.*, vol. 60, 2022, Art. no. 5522914.
- [37] J. Peng, Y. Huang, W. Sun, N. Chen, Y. Ning, and Q. Du, "Domain adaptation in remote sensing image classification: A survey," *IEEE J. Sel. Topics Appl. Earth Observ. Remote Sens.*, vol. 15, pp. 9842–9859, 2022.
- [38] P. V. Arun, I. Herrmann, K. M. Budhiraju, and A. Karnieli, "Convolutional network architectures for super-resolution/sub-pixel mapping of drone-derived images," *Pattern Recognit.*, vol. 88, pp. 431–446, Apr. 2019.
- [39] D. He, Y. Zhong, X. Wang, and L. Zhang, "Deep convolutional neural network framework for subpixel mapping," *IEEE Trans. Geosci. Remote Sens.*, vol. 59, no. 11, pp. 9518–9539, Nov. 2021.
- [40] X. Ma, Y. Hong, Y. Song, and Y. Chen, "A super-resolution convolutional-neural-network-based approach for subpixel mapping of hyperspectral images," *IEEE J. Sel. Topics Appl. Earth Observ. Remote Sens.*, vol. 12, no. 12, pp. 4930–4939, Dec. 2019.
- [41] Z. Liu, L. Zhao, X. Li, and S. Chen, "Linear feature detection for hyperspectral subpixel mapping," *Acta Geodaetica et Cartographica Sinica*, vol. 48, no. 11, pp. 1464–1474, Nov. 2019.
- [42] A. Villa, J. Chanussot, J. A. Benediktsson, and C. Jutten, "Spectral unmixing for the classification of hyperspectral images at a finer spatial resolution," *IEEE J. Sel. Topics Signal Process.*, vol. 5, no. 3, pp. 521–533, Jun. 2011.
- [43] H. V. Poor, *An Introduction to Detection and Estimation Theory*. Springer-Verlag, 1992.
- [44] Q. Wang, C. Zhang, X. Tong, and P. M. Atkinson, "General solution to reduce the point spread function effect in subpixel mapping," *Remote Sens. Environ.*, vol. 251, Dec. 2020, Art. no. 112054.